



# Particle flow numerical study of size effect on uniaxial compressive strength of natural building stone

Paraskevi Yiouta-Mitra · Konstantinos Svorakis · Pavlos Nomikos

Received: 18 June 2022 / Accepted: 12 December 2023  
© The Author(s) 2023

**Abstract** The fundamental influence of specimen size and micromechanical parameters on macroscopic structural behavior of natural building stone is investigated by particle flow numerical analysis. Laboratory tests of Dionysos marble cylindrical specimens under uniaxial compressive loading are simulated with a focus on the fracture development, failure mode and uniaxial compressive strength. Two series of simulations are performed with the PFC2D code, one to define the effects of different rates of deformation on the uniaxial compressive strength and fracturing of the specimens and the other to investigate the behavior of the specimens with the variation of five different parameters; platens velocity, specimen size, particle size distribution, standard deviation of randomized shear and normal strength as a micro-parameter and the ratio of shear to normal particle bonding strength. The specimen sizes also include rarely investigated smaller than NX dimensions. On selected specimens, the fracture development and the failure mode is depicted and discussed, and conclusions are drawn about the shear to tensile failure frequency and the crack patterns.

## Highlights

- Bonded particle numerical models provide vigorous insights of quasi-brittle rock microcracking development for previously uncharted specimen scale.
- The effects of micro-parameter selection in bonded particle numerical models are quantified with respect to the general behaviour and failure mode of the material.
- The detailed simulation with advanced particle flow code provides proof of the non-monotonous dependence of the UCS on the size of specimen.

**Keywords** Bonded particle model · Size effect · PFC · UCS · Failure mode · Tensile and shear microcracks

## 1 Introduction

The dependence of the compressive strength of quasi-brittle materials on the size and shape of a specimen is well-known and has been widely studied. The statistical nature of the distribution of flaws has been largely used to explain this dependence (Fisher and Tippett 1982, Weibull 1939). According to this theory, if two samples have different sizes but identical shapes, the probability of failure in the larger sample is higher than that of the smaller sample because it

---

P. Yiouta-Mitra (✉) · K. Svorakis · P. Nomikos  
School of Mining and Metallurgical Engineering, National  
Technical University of Athens, Athens, Greece  
e-mail: antipaxos@metal.ntua.gr

contains more flaws. As a result, the larger sample fails at a lower strength in comparison to the smaller sample, i.e. an increase in size causes a decrease in strength expressed as follows according to Wang et al. (2020) with reference to Weibull (1939) equation:

$$m \cdot \log \left( \frac{P(\sigma)}{P_{ref}(\sigma)} \right) = \log \left( \frac{V}{V_r} \right) \quad (1)$$

where  $P$  is the material strength,  $P_{ref}$  the strength of the representative sample,  $V$  the volume of the sample,  $V_r$  the volume of one element in the sample and  $m$  a material constant. A modified formulation of Eq. (1) was proposed by Hoek and Brown (1980) to predict the size effect in uniaxial compressive tests, depicted in Eq. (2):

$$C_0 = C_{0,50} \left( \frac{50}{d} \right)^{0.18} \quad (2)$$

where  $d$ =diameter,  $C_{0,50}$ =UCS for the specimen with diameter of 50mm,  $C_0$ =UCS of different size specimen.

The majority of the empirical and semi-empirical size effect models originated from or have a similar form to the statistical size effect model and are based on curve fitting with similar equations (Mogi 1962; Dey and Halleck 1981; Silva et al. 1993; Adey and Pusch 1999; Castelli et al. 2003; Yoshinaka et al. 2008; Darlington and Ranjith 2011; Zhang et al. 2011). They commonly follow an assumed size effect concept in which the strength reduces as the size increases (Wang 2020). An explanation of the decrease in bending strength by increasing the specimen sizes has also been given in terms of dimensional analysis; since the physical dimensions of strength ( $[Force][Length]^{-2}$ ) and toughness ( $[Force][Length]^{-1}$ ) differ, large specimens may be required to find the exact true values of material strength (Carpinteri 1989).

Other approaches include fracture energy theory and fractals. Bazant (1984) was the first to define a size effect model using fracture energy theory for quasi-brittle and brittle materials, known as the size effect law (SEL), by taking into account the role of energy for quantification of the crack growth and propagation. The Fractal Fracture Size Effect Law (FFSL) was later proposed by Bazant (1997) which considers the fracture surfaces in a number of materials such as rock, concrete, and ceramics to exhibit

fractal characteristics captured through the fractal dimension. Another fractal model was presented by Carpinteri et al. (1995) known as the multifractal scaling law (MFSL), as well as models presented by other researchers (e.g. Huang and Detournay 2008, Vileneuve et al. 2012).

The study of size effect is of undiminished importance since standard laboratory tests are carried out for specimens of dimensions of the order of 10–40 cm. These results are then “upscaled” for structures with dimensions many times larger than laboratory size. Since definite conclusions concerning the laws governing the transition region have not been reached, conclusions are still based on empirical or semi-empirical formulas obtained from curve fitting to the experimental results (Wang 2020).

In this research, a numerical bonded particle model of marble specimens is developed and subjected to uniaxial compression in order to simulate the fracture development and to examine the failure mode. A parametric analysis of several parameters influencing the uniaxial compressive strength and the modulus of elasticity is performed and the results obtained are compared to existing empirical relations. It is well known that the strength and deformational characteristics of a synthetic rock specimen of a bonded particle model depends on the strength and deformational microparameters of the bonds. For the bond model used in the current research, the main micro-parameters that are defined are the normal and shear bond strength and stiffness and also the stiffness of the contact between the particles. It has been suggested that other parameters such as the friction coefficient between the particles do not significantly affect the strength of the synthetic specimen but rather the post-peak behavior. Therefore, in the current study, the main micro-parameters selected to be examined are the ratio of the shear bond strength to the normal one and their statistical distribution, in relation to the loading rate of the specimen and its size.

## 2 Methodology

Significant advances in numerical modelling have been made in recent years with respect to the behavior and simulation of fractures. The development of discrete fracture networks combined to discrete element modelling or particle bonded modelling has

provided a very useful tool for the in-depth study of the effects of fracture intensity factors and size effects on fractured strong rock and quasi-brittle materials (Fan et al. 2023, Ma et al. 2023, Yiouta-Mitra et al. 2023, Bahrani and Kaiser 2016).

For the current research, the PFC2D simulation program (Particle Flow Code 2D) was selected for the numerical modelling because it has the ability to determine the mechanical properties, the microcracks and the failure of rocks, without any prior assumption for their behavior, by constructing bonded particle models, BPMs. The efficiency of the BPM for the simulation of the microscopic and macroscopic behavior of rocks in laboratory tests is known (Bahrani et al. 2014, Nomikos et al. 2020), even for complicated specimens and layouts. Although a 3-D simulation would capture in more detail the development of phenomena related to granular interactions, it is first necessary to study the size effect in two dimensions, for a better appreciation of the results. Further, since a 2-D investigation is much faster but—under the correct assumptions—equally meaningful, analyses in 2D are the optimum initial approach.

## 2.1 Contact model

The linear parallel bond model, LPBM, is used as the bonding model between the disk particles for the simulations of the current study. The LPBM simulates the mechanical behavior of cement like material between two adjacent particles in contact. Two sets of linear elastic springs normal and parallel to the contact plane, are used for the simulation of normal and shear stiffness of contacts and bonds. Normal and shear stresses develop with the relative movement of the particles in contact. The strength of bonds is provided by a shear and normal strength component. The bond breaks when the normal or shear stress surpasses the assigned strength. Then the behavior is governed solely by a frictional slip law between the particles in contact.

## 2.2 Model parameter selection and calibration

The assembly of the bonded particles is initially created in a material vessel that occupies the dimensions of the simulated specimen. The procedure for creating

the particle assembly in the code PFC2D is described by Potyondy and Cundall (2008). The bonding of particles is attained by applying suitably selected bond microparameters which translate into stiffness and strength of particles and their bonds. As a means of defining the parallel bond, it is necessary to set the values of normal and shear stiffness of contacts ( $k_n$ ,  $k_s$ ) and bonds ( $\bar{k}_n, \bar{k}_s$ ), which relate to their effective moduli,  $E^*$  for contacts and  $\bar{E}^*$  for bonds and their respective normal to shear stiffness ratios,  $\kappa^* = k_n/k_s$  for contacts and  $\bar{\kappa}^* = \bar{k}_n/\bar{k}_s$  for bonds. The strength of bonds is determined by the tensile ( $\bar{\sigma}_c$ ) and shear ( $\bar{\tau}_c$ ) strength of the bonding cement. The friction coefficient ( $\mu$ ) between the particles defines the slip limit after bond fracture. In addition, for the development of the particle assembly, the minimum radius of disk particles  $R_{\min}$  and the ratio of maximum to minimum radius  $R_{\max}/R_{\min}$  must also be determined.

The selection of the model microparameters affects both the macroscopic mechanical properties of the synthetic material under loading as well as the failure mode of the numerical specimen. The moduli of the contacts and the bonds are associated with the modulus of elasticity of the material and the ratio of normal to shear stiffness is associated with the Poisson's ratio of the material. This is achieved by setting high values for the bond strength of the material so that it behaves elastically. However, the selection of the bond strengths must subsequently be adapted. Further, by setting and differentiating the values of  $E^* = \bar{E}^*$ , UCS tests are performed until the model's modulus of elasticity is equal to the laboratory modulus of elasticity. Finally, by setting and differentiating the values of SBS and NBS, UCS tests are performed until the model's UCS also, is equal to the UCS defined in the laboratory.

The ratio of the shear bond strength to the normal bond strength (SBS/NBS) actually affects the development of shear and tensional microcracks, i.e. the failure mode of the bond. According to Yoon (2007), a more realistic simulation is obtained when SBS/NBS=2. On the other hand, a setting of SBS=NBS, reveals more clearly the crack mechanisms which are activated by shear microcracking and the following shear deformation along the crack direction (Potyondy & Cundall 2004). In this research, both settings have been explored.

**Table 1** Values used for the parametric analyses of the uniaxial compressive strength tests with the PFC code

Parameter	Values				
Specimen size (H) in mm	60	100	120	300	400
Velocity (v) in mm/s	25	41.7	50	125	166.7
Ratio SBS/NBS (r)	1	2			
STD of normal distribution for shear and normal bond strength in MPa	None (deterministic)	10	20		
Particle size distribution (PSD)*	I	II	III	IV	

\*The particle size distribution was based on different seed values

### 3 Numerical analyses

Uniaxial compression test (UCS) simulations were conducted on specimens of Dionysos marble with a ratio of height to diameter,  $H/D=2$ , with PFC2D simulation program. Their heights were 60mm, 100mm, 120mm, 300mm and 400mm, and their diameters were 30mm, 50mm, 60mm, 150mm and 200mm. The minimum radius of the disk particles  $R_{\min}$  was 0.5mm, the ratio of the maximum to minimum radius  $R_{\max}/R_{\min}$  was 1.5 and the friction coefficient was set equal to 0.577. In addition, the normal to shear stiffness ratio for the contacts and the bonds was set equal to 2 ( $\kappa^* = \bar{\kappa}^* = 2$ ,  $\kappa^* = k_n/k_s$  for the contacts and  $\bar{\kappa}^* = \bar{k}_n/\bar{k}_s$  for the bonds). The macroscopic uniaxial compressive strength was selected based on the results of laboratory tests on Dionysos marble by Vardoulakis et al. (2002) as  $UCS_{\text{lab}} = 103\text{MPa}$ . This value was taken as an average of the UCS experimental values. For the modulus of elasticity, a continuous reduction with increasing axial strain is described in Vardoulakis et al. (2002) where the range of  $E_{t,\text{lab}}$  values varies between 80 and 60GPa. Therefore the value of 72.3GPa was selected for the current study. Friction between the loading platens and the specimen took into consideration the use of a lubrication system.

According to the previous paragraph 2.2, the values of ratio SBS/NBS were selected to be 1 and 2, so as to obtain the different behavior described by each case. As a result, two sets of simulations were conducted. Obviously, for each set of simulations, a different calibration was required. In the simulations with SBS/NBS = 1, the effective moduli  $E^* = \bar{E}^*$ ,  $E^*$  for the contacts and  $\bar{E}^*$  for the bonds, were determined as equal to 37.85 GPa and the SBS = NBS = 39.47MPa. For the simulations with SBS/NBS = 2, the effective moduli  $E^* = \bar{E}^*$  were determined equal to 37.87GPa, the SBS = 62.8MPa and the NBS = 31.4MPa. Those

values provided the best possible approximation of the aforementioned rockmass laboratory modulus of elasticity and UCS. The calibration process was carried out on the specimen sizes of 120mm x 60mm (H120W60) and the numerically obtained modulus of elasticity varies between 72.0 and 73.0 for the model series, while the detailed comparison of numerical and laboratory UCS for the various model series is provided in Table 6.

For both SBS/NBS ratios, the effect of three different parameters was examined; the rate of deformation, the randomness of the particle size and the randomness of the bonding particle strength. The implementation was performed by two series of experiments:

*Series A:* Models with variable deformation rate and constant velocity of  $v=50\text{mm/s}$  for the compressive platens of the specimen and variable ratio SBS/NBS. This series was performed with a view to compare to models of constant deformation rate and thus obtain the effects of different rates of deformation on the UCS and fracturing of the models. The variable deformation rates refer specifically to the mechanical loading rate of the specimen. This is the result of applying a constant velocity on the top wall and a zero velocity on the bottom wall of the model, that simulate the loading platens of the synthetic specimen, while the height of the specimens varies.

*Series B:* Models based on the variation of five parameters; size of specimens (5 values), velocity of the platens (5 values, one for each size so as to maintain the same rate of deformation), ratio of shear to normal bonding strength (2 values), standard deviation of shear and normal bonding strength of particles for normal distribution of their values (3 values), randomness of the particle size (4 values). Table 1 contains all the information concern-

ing this series of experiments and the related variables.

For the calculation of the velocity of the compressive platens of the specimens, so that the same rate of deformation is preserved, the following equation was used:

$$v(H) = \left( \frac{50\text{mm/s}}{120\text{mm}} \right) \times H(\text{mm})$$

In total, 130 numerical analyses were performed. In the following, in order to refer to a specific test according to Table 1, coded names are given to each experiment, as in the examples:

- For specimen size  $H=300$  mm, velocity  $v=125$  mm/s, ratio  $\text{SBS/NBS}=1$ , standard deviation  $\text{STD}=\text{none}$  and particle size distribution PSD category I: H300\_v125\_r1\_PSD-I
- For specimen size  $H=100$  mm, velocity  $v=41.7$  mm/s, ratio  $\text{SBS/NBS}=2$ , standard deviation  $\text{STD}=10$  MPa and particle size distribution PSD category IV: H100\_v41.7\_r2\_STD-10\_PSD-IV

## 4 Results

The output of the analyses was the uniaxial compressive strength UCS in MPa and the mean modulus of elasticity in GPa. Figure 1 contains the stress–strain diagram in green and overlapping with the image of a specimen. Therefore, the horizontal axis is not the specimen dimension but the strain values from the stress–strain curve. Similarly, the vertical axis contains the stress values. In the body of the specimen, the grains are depicted in blue, tensional cracks are depicted in black and shear cracks in red.

Uniaxial compressive strength, UCS, and modulus of elasticity,  $E$ , for specimen H400\_v166.7\_r1\_STD-10\_PSD-III were 92.1MPa and 65.9GPa respectively. All over the specimen's body tensional and shear cracks can be found (Fig. 1). All cracks expand diagonally from the two sides of the specimen to the base of it. In addition, tensional and shear cracks are pronounced on the upper side of the specimen. Most dominant, on this specific specimen, are the tensional cracks.

### 4.1 Fracture development

In this paragraph the initiation and the development of the fractures will be presented based on a selection of the most characteristic results. Therefore, only the shear and tensional cracks will be depicted on the specimens. Figure 2 contains the fracture process of one of the smaller specimens with equal shear and normal bonding strengths, H100\_v41.7\_r1\_PSD-III.

At first (Fig. 2a), a few tensional cracks on various locations on the specimen's body are visible. Then, in Fig. 2b on the bottom side of the specimen a cluster of tensional cracks start to form. The failure of the specimen comes when the aforementioned tensional cracks expand as far as the base of the specimen, with the simultaneous formation of a few shear cracks as well.

In the following Fig. 3, the fracture process of the next size specimen H120\_v50\_r1\_PSD-IV is depicted.

Again, a few tensional and shear cracks are created on several parts of the specimen. Then, mostly tensional but also some shear cracks can be seen in the center expanding diagonally downwards, on the lower left side and on the base of the specimen. The specimen fails when the aforementioned cracks expand even more and connect with each other forming at the same time a big diagonal crack from the right side to the base of the specimen.

Next, some of the larger specimens will be presented, starting with Fig. 4 which contains the fracture process of a specimen with ratio of shear to normal bonding strength equal to 2, H300\_v125\_r2\_PSD-I.

As expected, there are differences due to the size. In the beginning, tensional cracks are visible all over the specimen's body, but they are more pronounced on the top and left upper side and on the bottom of the specimen. Then the cracks on the upper side expand and connect in order to form a cluster of tensional cracks. In addition, tensional cracks can be found expanding from the center and the right side of the specimen to its base. The failure of the specimen occurs when all the aforementioned tensional cracks expand and connect at the center of the specimen and on multiple directions.

Finally, one of the largest specimen series is depicted in Fig. 5 and contains the fracture process of specimen H400\_v166.7\_r2\_PSD-II.

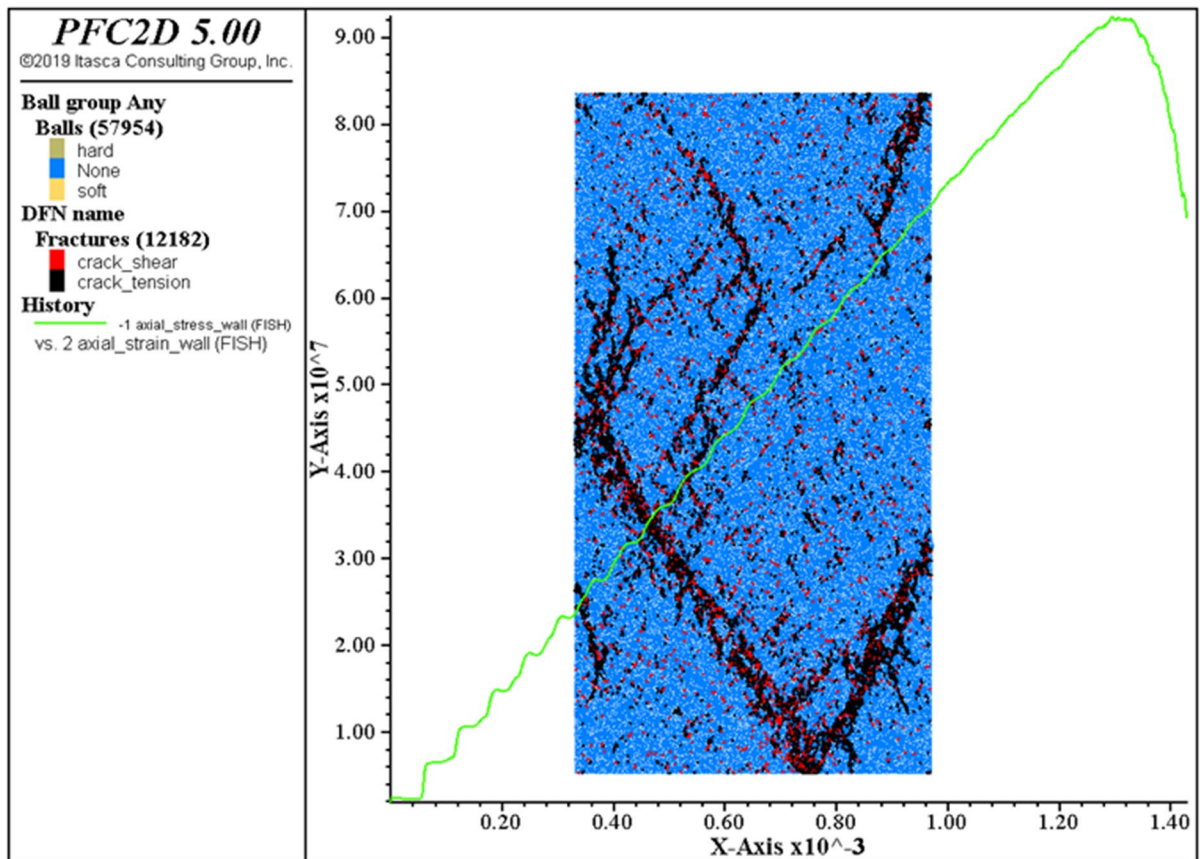


**Fig. 1** Cracks, failure mode and stress–strain curve of specimen H400\_v166.7\_r1\_STD-10\_PSD-III

Clearly in Fig. 5a, the tensional cracks are dispersed all over the specimen's body. The right bottom edge is an area with apparent larger crack concentration. Then, in Fig. 5b all cracks expand diagonally towards the center with a simultaneous expansion of the tensional cracks on the upper left side of the specimen. The specimen fails when the tensional cracks expand and connect on the center and on multiple directions.

All cracks developed when peak strength was attained. Similar fracture developments have been observed on all specimens of the same size, shear to normal bonding strength ratio, and particle size distribution for each occasion. In the case of randomized shear to normal bonding strength ratio, especially for the larger specimens and the higher strength deviation from the mean value, a greater dispersion of microcracks before the peak strength was observed.

#### 4.2 Specimen failure

The numerical analyses provided the means to observe the diversification of the failure mode. To this end, a selection of the specimens' final state in failure is depicted and commented on in this paragraph.

Table 2 showcases the final state with the fully developed cracks and clearly visible failure mode of PSD category I specimens with SBS/NBS=1 and constant velocity vs variable velocity. For all cases, the tensional cracks outnumbered by far the shear cracks. However, for the last 3 larger specimen sizes the amount of shear cracks was more pronounced.

Observing the patterns of failure for the selected specimens and comparing the cases of variable and constant velocity, it is noted that the cracks for size H60, are found in the center and expanding diagonally to the base of the specimen. In the case of

**Fig. 2** Fracture development of specimen H100\_v41.7\_r1\_PSD-III

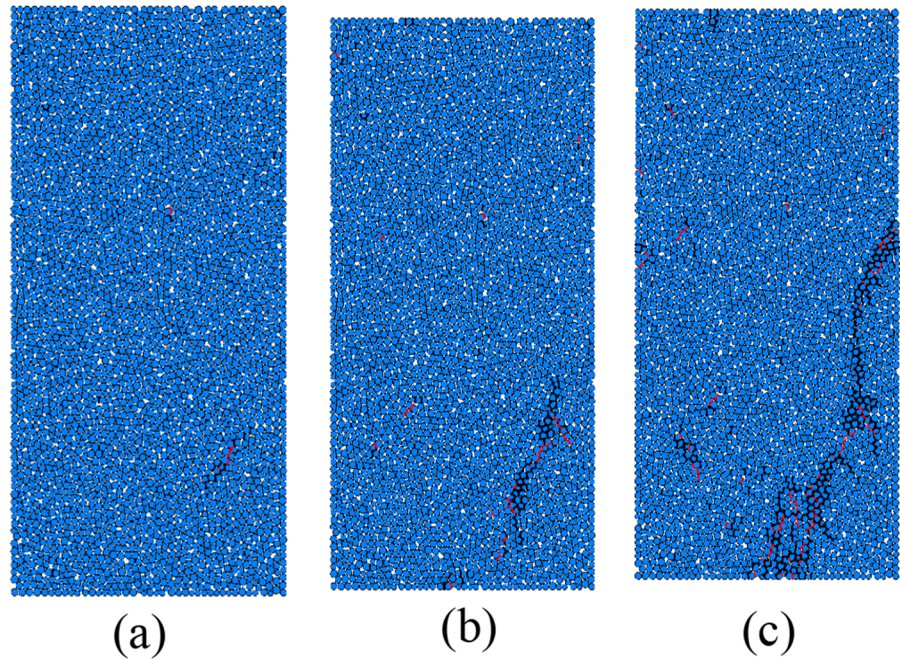
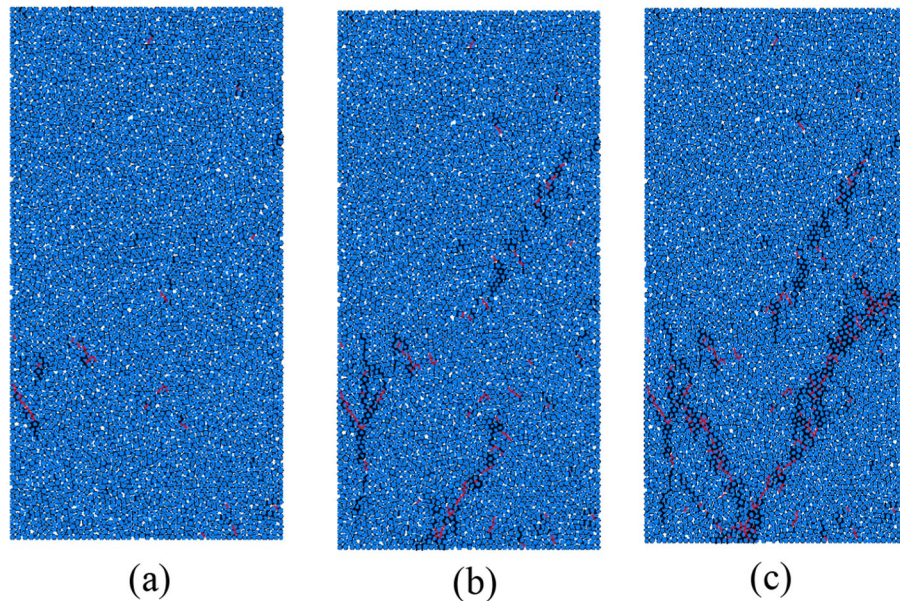


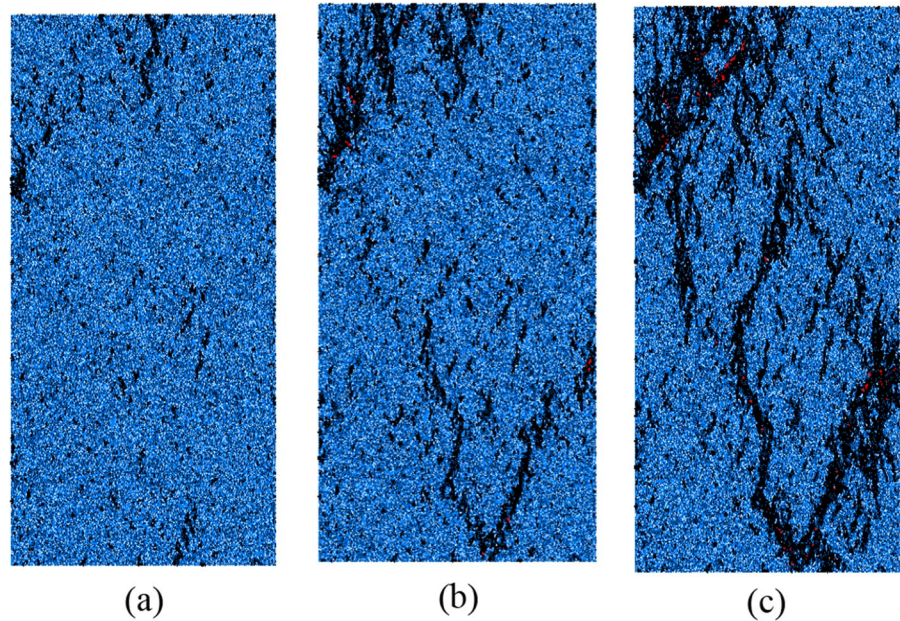
**Fig. 3** Fracture development of specimen H120\_v50\_r1\_PSD-IV



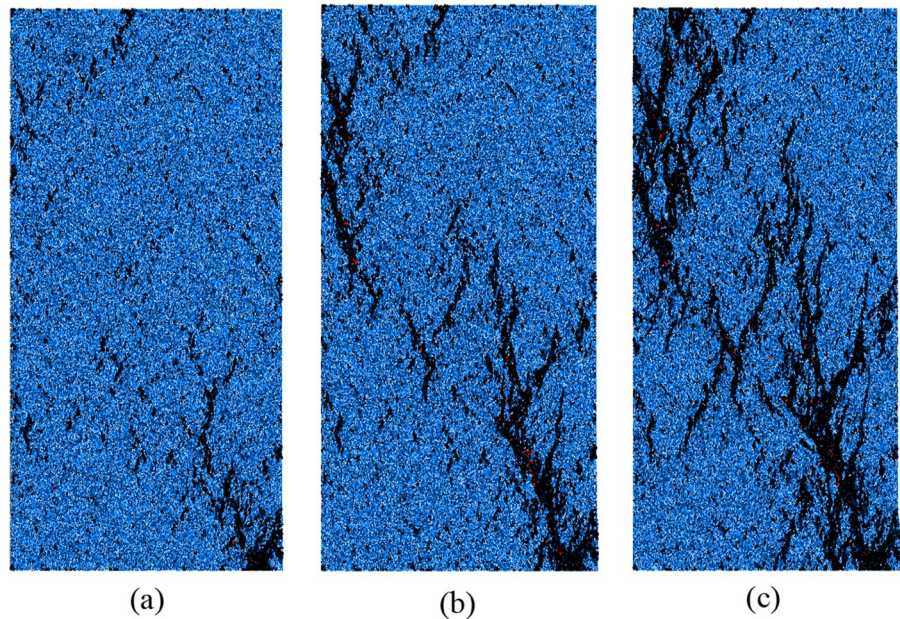
H100 size, most cracks are found on the upper side of the specimen. In specimen size H120, the cracks are expanding from the upper side to the center of the specimen. For size H300, most cracks are found on the upper side of the specimen. Evidently, the crack pattern for all these specimens is not very sensitive to the loading rate. In specimen size H400 however, in

the model with the constant velocity most tensional cracks are concentrated in the area from the base to the center of the specimen, in contrast to the model with variable velocity where the cracks are found at multiple directions. Shear cracks that appeared in all specimens contained in Table 2 with constant and

**Fig. 4** Fracture development of specimen H300\_v125\_r2\_PSD-I



**Fig. 5** Fracture development of specimen H400\_v166.7\_r2\_PSD-II



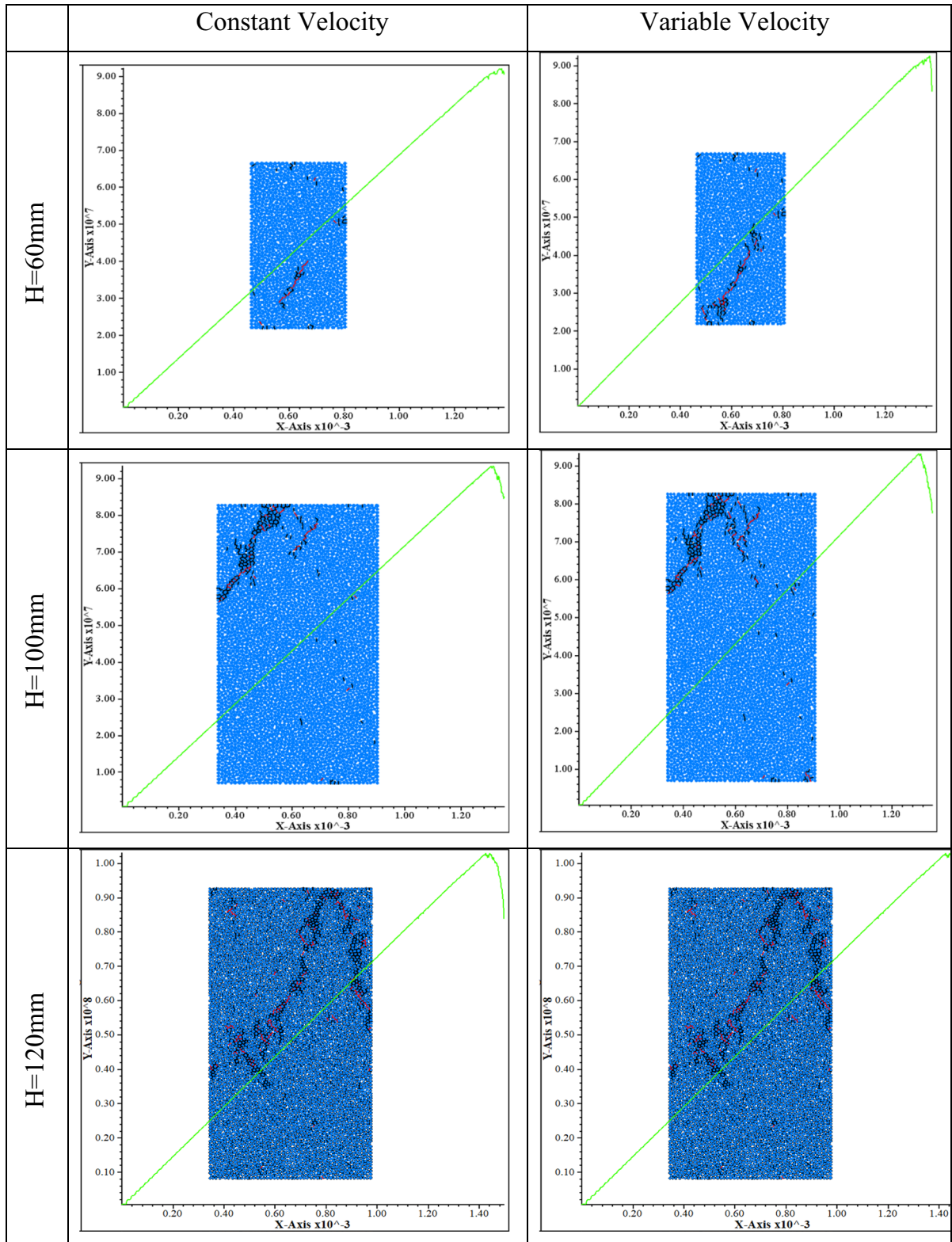
variable velocity were few as compared to the tensile ones. In average 17% of the total number of cracks that developed were due to shearing failure.

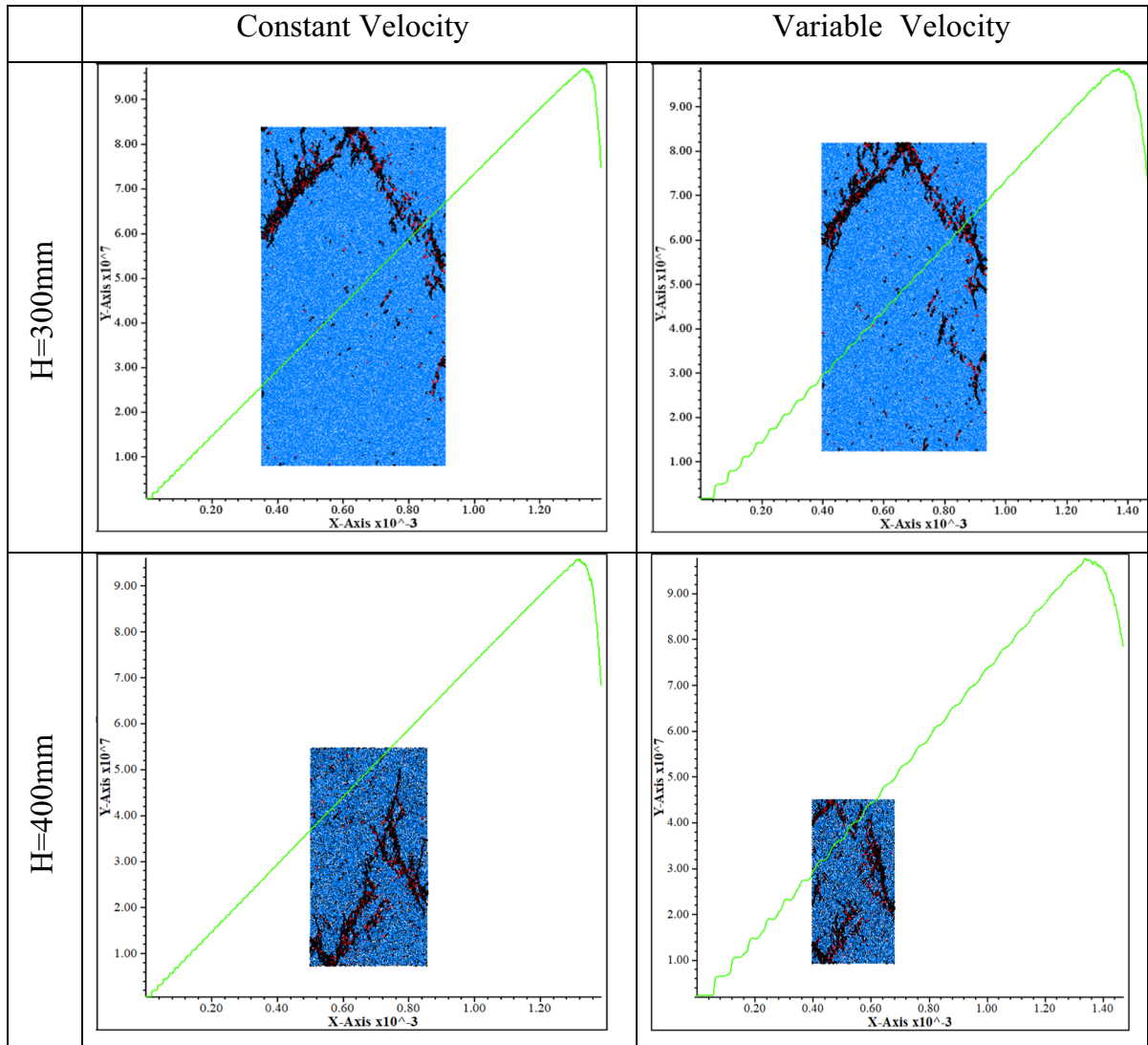
Table 3 showcases the cracks and failure mode of PSD category I specimens with SBS/NBS=1 and standard deviation, STD=10MPa vs STD=20MPa. The cracks are more scattered on specimens with

STD=20MPa. There is a variance on their strengths as well. As the specimens get larger, the cracks are more scattered. For the first 3 specimen sizes the crack pattern is similar for specimens with constant vs variable velocity. For the two larger specimen sizes, the crack pattern is differentiated among them and more shear cracks can be seen in contrast to the



**Table 2** Final State—Cracks and failure mode for PSD category I specimens with SBS/NBS=1 and constant velocity vs variable velocity



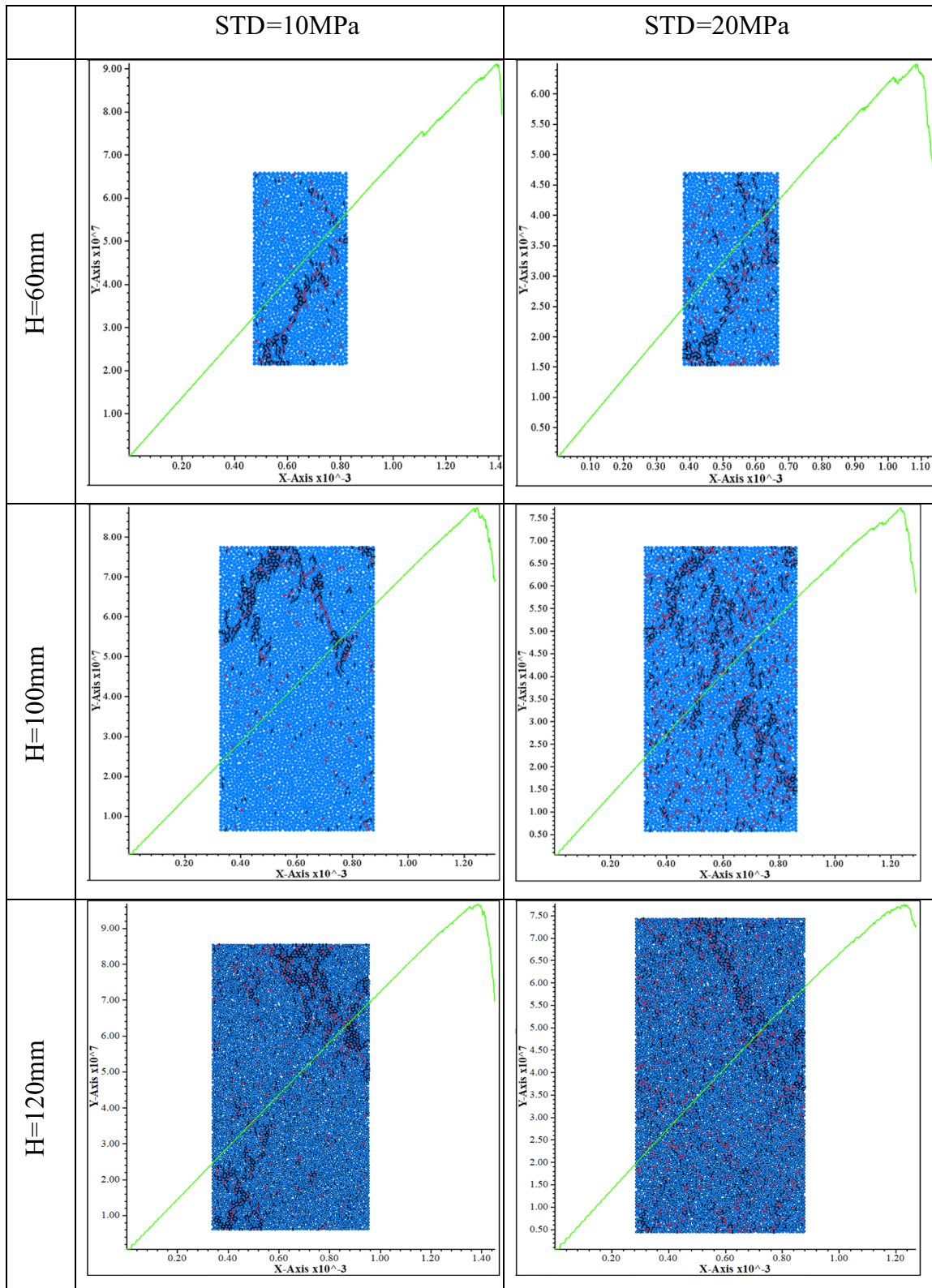
**Table 2** (continued)

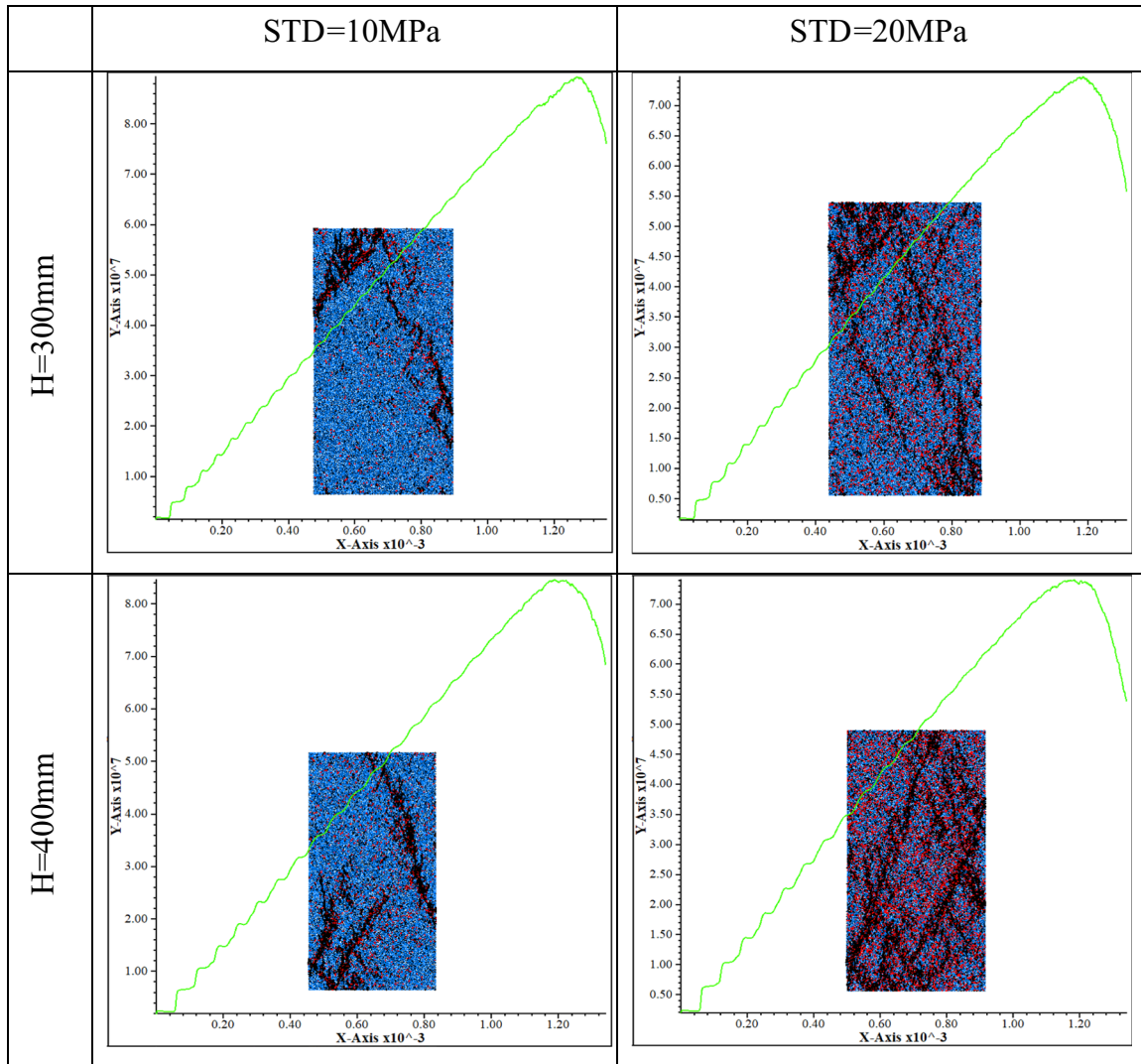
smaller specimens. For all cases tensional cracks outnumbered the shear cracks, leading to the specimens' failure. There is actually a clear trend of shear cracks appearing slightly more frequently as the standard deviation augments, as will be explained later on, in Fig. 7. In specimens with  $STD = 10\text{MPa}$ , shear cracks are in average 24% of the total cracks, in contrast to specimens with  $STD = 20\text{MPa}$ , where the shear cracks rise up to an average of 38% of total cracks appearing on the specimens.

Table 4 showcases the cracks and failure mode of PSD category I specimens with  $SBS/NBS = 2$  and constant velocity vs variable velocity. For all

specimen sizes tensional cracks outnumber by far the shear cracks. On smaller specimens, crack pattern is similar among them, in contrast to larger specimens, where the crack pattern is differentiated for specimens with constant vs variable velocity. It is further concluded that the crack pattern is not sensitive to the velocity. In comparison to PSD category I specimens with ratio of shear to normal bond strength equal to 1, different failure patterns are detected and only tensional cracks lead to the failure of the specimens. As expected for both constant and variable velocity occasions, shear cracks only take 1% of the total number of cracks on the specimens since the ratio of the shear

**Table 3** Final state—Cracks and failure mode for PSD category I specimens with SBS/NBS=1 and standard deviation, STD=10MPa vs STD=20MPa



**Table 3** (continued)

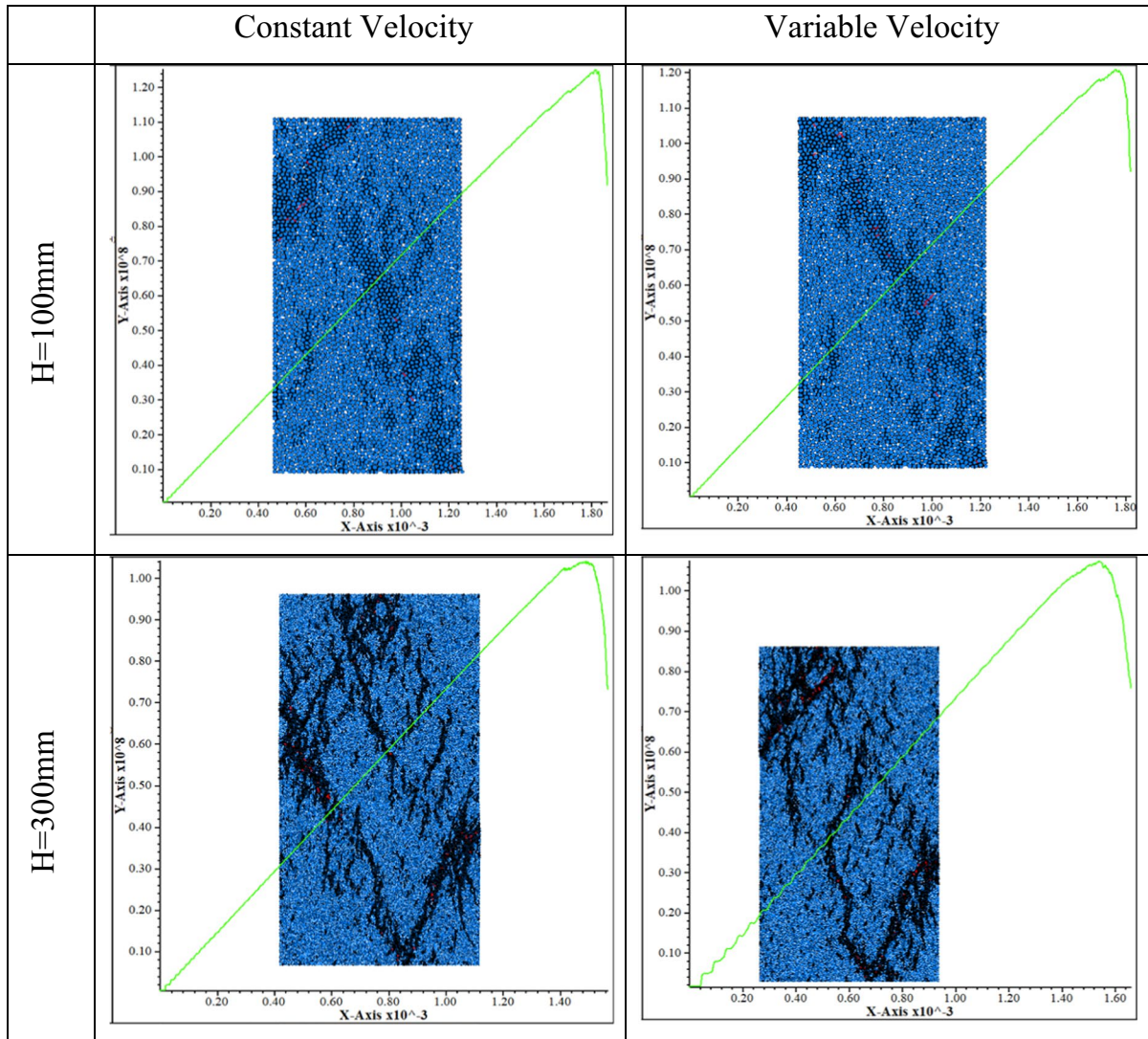
to normal bonding strength gives precedence to tensile failure.

Table 5 showcases the cracks and failure mode of PSD category I specimens with SBS/NBS=2 and standard deviation, STD=10MPa vs STD=20MPa. For all specimen sizes, the general crack pattern is differentiated for specimens with different STD in their strength distributions. The tensional cracks clearly outnumber the shear cracks and they lead to failure. According to Fig. 7 shear cracks for STD=10MPa is 1% and for STD=20MPa is less than 5% of the total number of cracks. By increasing the size of the specimens, more tensional cracks are visible. In comparison to specimens with ratio of shear to normal bond

strengths equal to 1, the general crack pattern is different. Further, the similarly appearing in smaller quantities shear cracks, are now very few compared to the higher percentage observed for the specimens with equal shear and normal bonding strength. In all occasions of course it is the tensional cracks that lead to the specimen failure.

Figure 6 contains the summary of all shear crack failures with respect to the total number of crack failures. As already observed, the results can be divided in three basic areas, the highest being around 40% shear/total fracture number for the specimens with the highest strength variability and equal shear to normal bonding strength. The second area is around 20% of

**Table 4** Final state—Cracks and failure mode of PSD category I specimens with SBS/NBS=2 and constant velocity vs variable velocity



shear/total fracture number for the majority of the specimens. Finally, the lowest participation of shear fractures in the specimens was observed for the SBS/NBS=2 test series.

**5 Discussion**

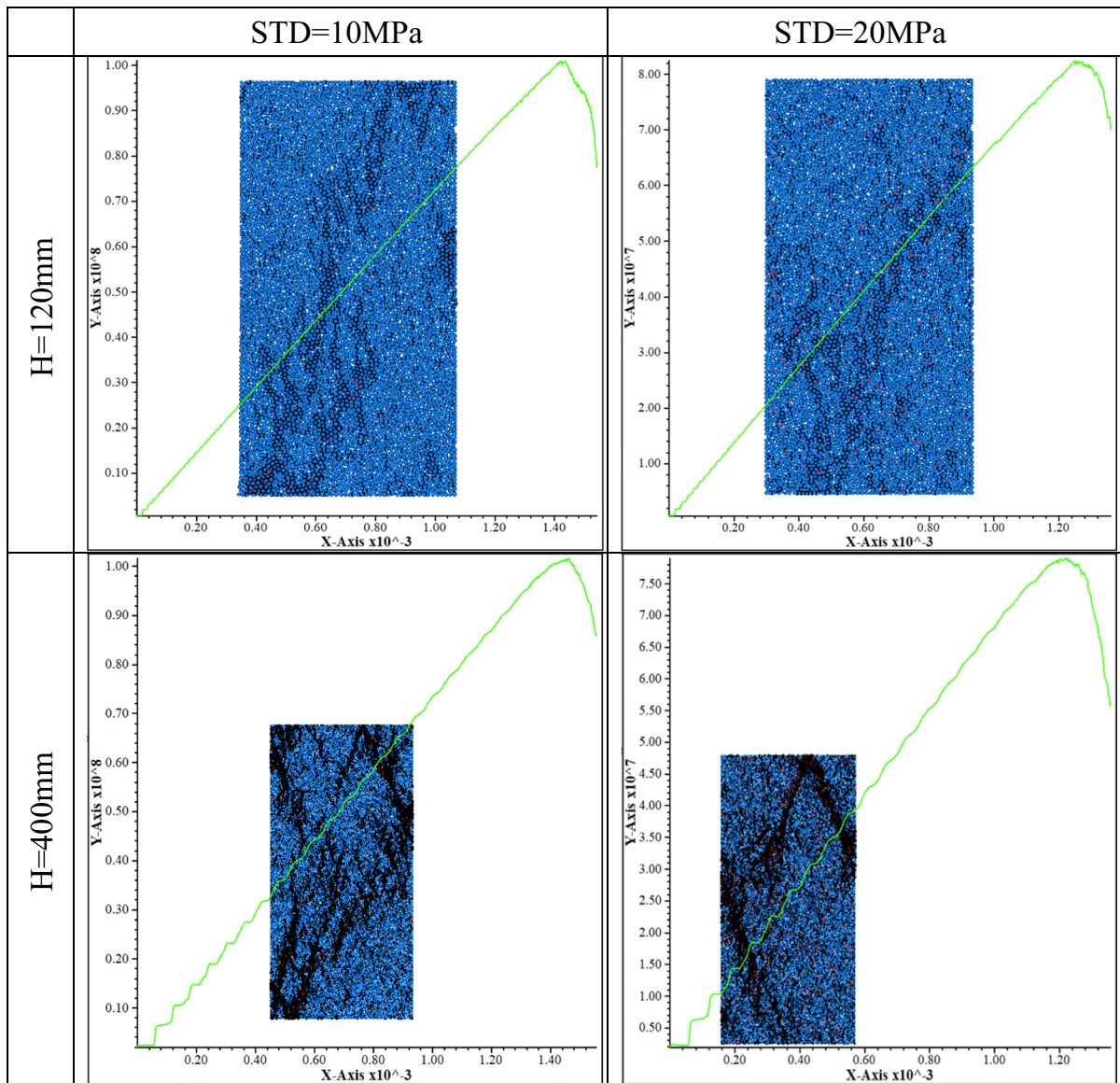
For the calculation of the UCS, the empirical equations of Hoek & Brown 1980, (Sect. 1, Eq. 2) and Martin et al. 2011 (Eq. 3), were used, in order to compare the empirical approach to laboratory and numerical results.

$$UCS = 0.81 + \frac{0.4}{\exp\left(\frac{D}{1.21}\right)} \tag{3}$$

where D=the normalized diameter.

The combined UCS results of the numerical models for both ratios SBS/NBS and the laboratory tests are summarized in Table 6. According to this table, the range of UCS strength values calculated in the numerical models is 68.7MPa to 103MPa for SBS/NBS=1 ratio and 76.5MPa to 125.1MPa for SBS/NBS=2 ratio. The empirical Eqs. (2) and (3) are also

**Table 5** Final state—Cracks and failure mode of PSD category I specimens with SBS/NBS=2 and standard deviation, STD=10MPa vs STD=20MPa



included and have been computed with a value of  $C_{0,50}$  equal to the one measured by the H100 series with steady deformation rate of the numerical experiments. It is also noted that the numerical values are the average of the four particle size distributions PSD I to IV results. Figures 7 and 8 contain a graphical representation of the comparison of all results.

According to Figs. 7 and 8 the dependence of the UCS on the size of the numerical specimens is non monotonous. This is in agreement with the laboratory

results. With respect to the size effect, the laboratory results are more sensitive than the numerical results.

The empirical Eqs. (2) and (3) attribute linear dependency of the UCS to the size of the specimens. While the specimen size is increasing, the UCS strength is decreasing. The size effect considered by these equations is less pronounced compared to the laboratory results.

**Fig. 6** Ratio of shear to total cracks for all PSD-I specimens for both SBS/NBS ratios

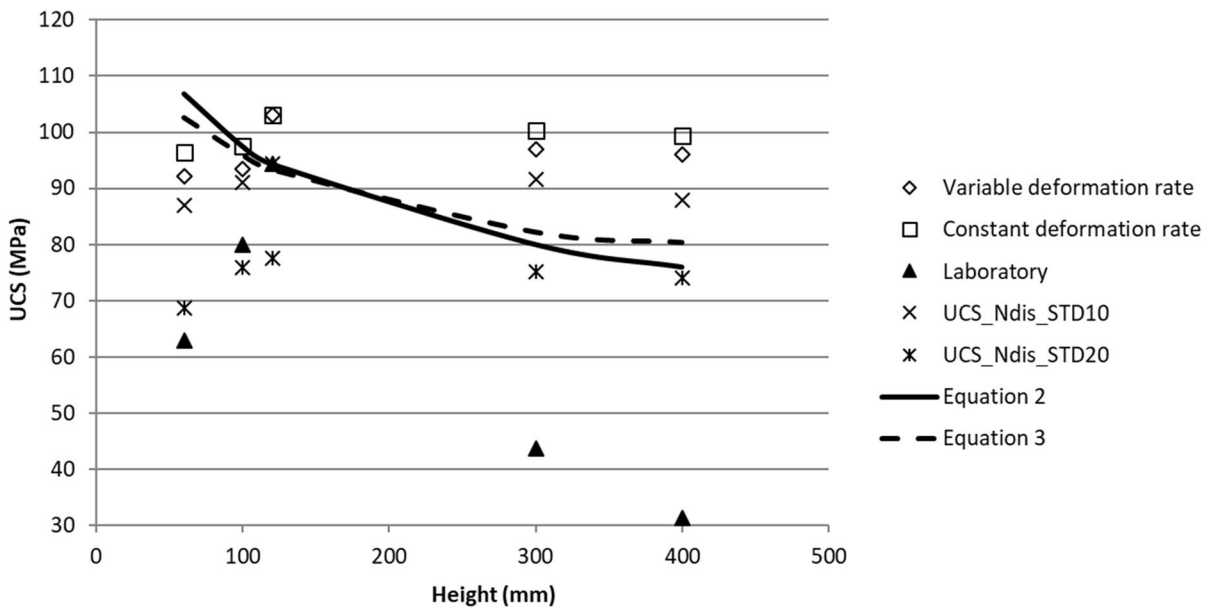
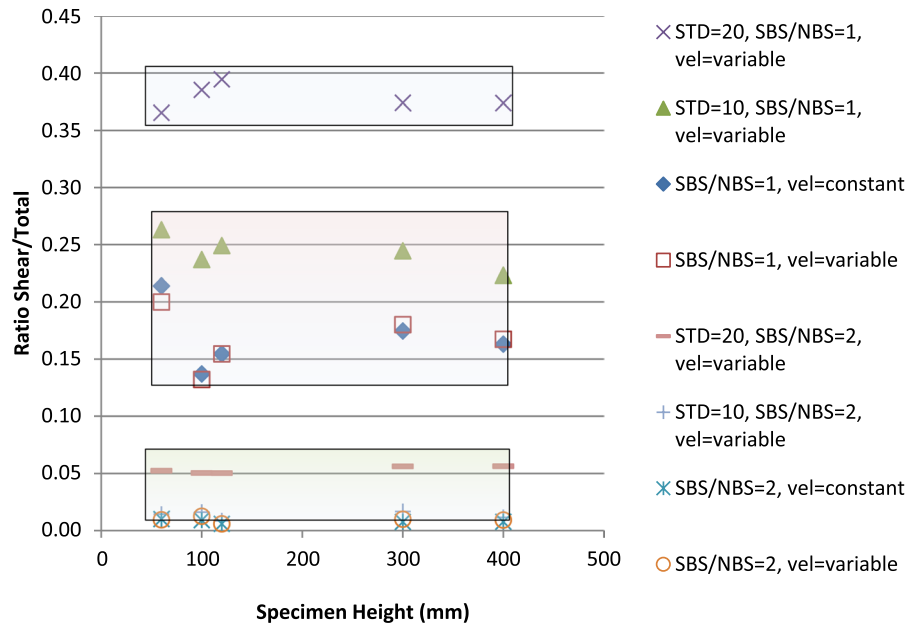


**Fig. 7** Graph of combined UCS results for specimens with SBS/NBS = 1,  $C_{0.50}$  = UCS of H100 specimen with variable velocity

Comparing the results from the empirical equations to those from the numerical analysis for both SBS/NBS ratios more trends appear. Obviously, Eq. (2) results for specimen size H100 have the best agreement for all numerical cases. H120\_v50\_r1\_STD-10 specimen's UCS is quite close to both the

empirical as well as the laboratory results. Similarly, H120\_v50\_r2, H120\_v50\_r2\_PSD-I and H120\_v50\_r2\_STD-10 specimens' results are in agreement with empirical relations as well. However, for bigger specimen sizes there is a considerable difference in UCS results for both SBS/NBS ratios.

**Table 6** Combined UCS results with both SBS/NBS ratios

SBS/NBS H(mm)	i		ii		iii		iv		v		vi		vii	
	1	2	1	2	1	2	1	2	1	2	1	2	1	2
60	62.9	92.1	113	96.4	108.8	87	93.9	68.7	76.5	106.8	128.2	102.6	123.2	
100	80	93.4	125.1	97.4	116.9	91.1	105.7	75.9	81.9	97.4	116.9	96	115.2	
120	94.3	103	103	103	107.8	94.4	101.8	77.6	81.5	94.3	113.1	93.4	112	
300	43.8	97	104.1	100.2	107.8	91.7	104.6	75.1	84.8	79.9	95.9	82.2	98.6	
400	31.4	96	105	99.5	108.8	87.9	104.8	74	80.7	75.9	91.1	80.3	96.4	

where

(i): Laboratory UCS (MPa)

(ii): Variable deformation rate UCS (MPa)

(iii): Constant deformation rate Average UCS (MPa)

(iv): Constant deformation rate Average UCS, Normal distribution with standard deviation 10MPa for shear and normal bond strengths (MPa)

(v): Constant deformation rate Average UCS, Normal distribution with standard deviation 20MPa for shear and normal bond strengths (MPa)

(vi): Equation (2) UCS for  $C_{0.50}$  equal to variable velocity results (MPa)

(vii): Equation (3) UCS for  $C_{0.50}$  equal to variable velocity results (MPa)

In order to classify the critical stress level for specimen damage initiation, the overall specimen axial stress when the first tensile bond breakage occurred has been extracted from the numerical models. The tensile stress level for damage initiation in the specimen depends on the normal bond strength, which in the simulations with SBS/NBS=1 was set at 39.47MPa. For the simulations with SBS/NBS=2, the shear bond strength was 62.8MPa and the normal 31.4MPa. Therefore, these values constitute the critical levels of the tensile strength at the microcracking level, i.e. the bond tensile stress level required for bond breakage. The average axial stress level across the entire specimen the moment that the first tensile bond breakage occurs is a value that has to be extracted from the simulations. It is the macroscopic stress and is therefore comparable to the peak compressive strength presented in the previous Table 6. Table 7 contains the dimensionless values of the onset of the first tensile bond breakage as compared to the peak compressive stress, i.e. their ratio.

According to these results, the first tensile bond breakage occurs over a large span of values; between 1 and 87 percent of the specimen strength. There are pronounced differences between the 8 sets of experiments. Looking at the classification of Table 7 columnwise, the specimens with practically immediate occurrence of first bond breakage were the ones with the normally distributed bond strength, i.e. columns III and IV, the latter being the most intense. On the other side of the specter were the specimens loaded at variable deformation rate of column I. As far as the different shear to normal bond strength ratios are concerned, the higher SBS/NBS cases exhibited faster occurrence of the first bond breakage, which means that specimens depicting easier development of tensional microcracks, also crack faster. Finally, considering the specimen size, there is non-monotonous behavior for all cases.



**Table 7** Ratio of axial stress level for first tensile bond breakage to the peak compressive strength

SBS/NBS H(mm)	I. Variable deformation rate		II. Constant deformation rate		III. Normal distr. SDEV 10		IV. Normal distr. SDEV 20	
	1	2	1	2	1	2	1	2
60	0.61	0.36	0.71	0.49	0.32	0.24	0.01	0.02
100	0.87	0.52	0.63	0.42	0.29	0.04	0.01	0.01
120	0.67	0.53	0.66	0.50	0.16	0.07	0.01	0.01
300	0.65	0.48	0.56	0.41	0.07	0.02	0.02	0.02
400	0.57	0.42	0.53	0.39	0.03	0.02	0.03	0.03
Average	0.67	0.46	0.62	0.44	0.17	0.08	0.02	0.02

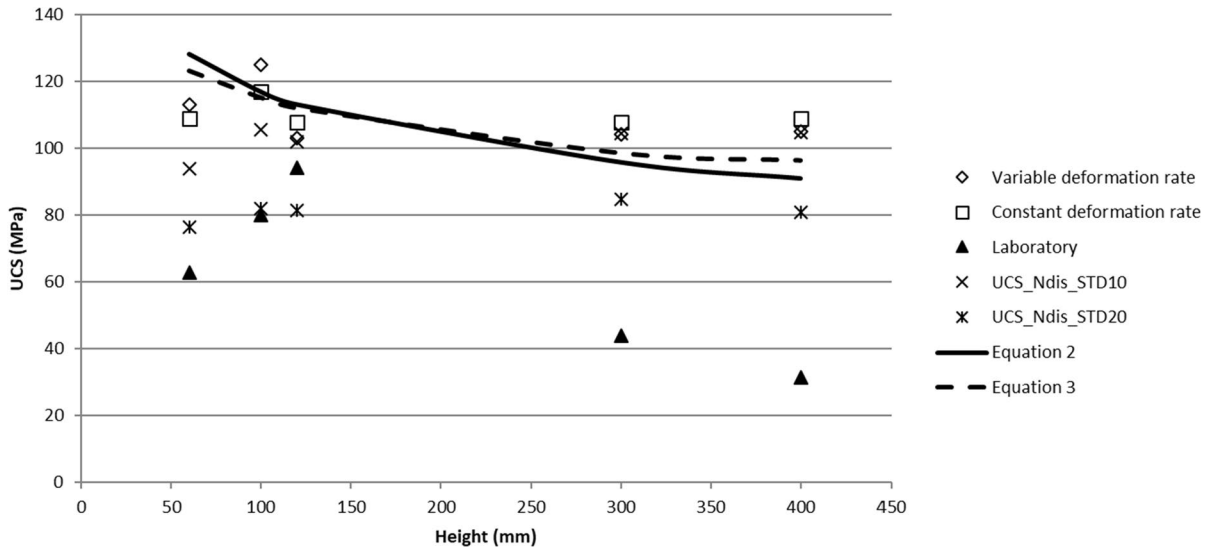


**Fig. 8** Graph of combined UCS results for specimens with SBS/NBS=2,  $C_{0,50}$ =UCS of H100 specimen with variable velocity

### 6 Conclusions

Detailed simulation of the fracture phenomenon of specimens under uniaxial compressive stress has been performed by use of the particle flow code PFC2D. The fracture development, the failure mode and the uniaxial compressive strength are investigated by means of two series of experiments; the first one with constant platens velocity so as to define the effects of different rates of loading (i.e. deformation rate) on the UCS and fracturing of the models. The second series of simulations is performed with constant rate of deformation, i.e. variable velocity for each specimen size, so as to draw conclusions about the behavior of the specimens with the variation of five different parameters; platens velocity, specimen size, particle size

distribution, standard deviation of normal distribution of shear and normal strength as a micro-parameter and the ratio of shear to normal particle bonding strength.

The most important observations are hereby summarized:

1. In terms of microscopic failure modes, the patterns show all specimens to have failed primarily in tension and partly in shear.
2. The specimens with the highest participation of shear cracking were the ones with equal shear to normal particle bonding strength and the highest variability in bonding strength as a micro-parameter.
3. In terms of macroscopic failure modes the main pattern was shearing along inclined planes

formed by accumulation of tension micro-cracks. More rarely, failure appeared along axially formed fractures.

4. For small specimen sizes, crack patterns are similar in both occasions of shear to normal bonding strength ratios. Larger specimen sizes exhibit different crack patterns for both SBS/NBS ratios.
5. The dependence of the UCS on the size of the numerical specimens is non monotonous. An initial increase of UCS with increasing specimen size is observed, with a peak UCS for the specimen with  $H=120$  mm, followed by a decrease of the UCS when the specimen size increases to  $H=400$  mm. This is also observed in the laboratory results of the specific rock, where the dependence of the UCS is similarly non monotonous, noticing however, that the size effect is much more pronounced.
6. Monotonous dependency of the UCS on the size of the specimens is described by the empirical Eqs. (2) and (3), in contrast to the laboratory tests and the numerical simulations.
7. The size effect is less pronounced for both the empirical equations as well as the numerical experiments, in contrast to the laboratory test results.
8. The variation with respect to the constant deformation loading rate was found to affect slightly the strength of the specimen and the associated crack development, while the final crack distribution across the entire specimens is very similar between the two series.
9. The stress level at first bond breakage varies significantly across all five parameters that have been studied. The greatest effect is caused by the assumption of the bond strength distributions, followed by the rate of deformation (loading) and lastly, by the shear to normal bond strength ratio.

**Author contributions** PN and PYM contributed to the study conception and design. Material preparation, data collection and analysis were performed by KS and PYM. The first draft of the manuscript was written by PYM and KS and all authors commented on the final version of the manuscript.

**Funding** Open access funding provided by HEAL-Link Greece.

**Data availability** The datasets generated during and/or analysed during the current study are available from the corresponding author on reasonable request.

#### Declarations

**Competing interests** On behalf of all authors, the corresponding author states that there is no conflict of interest.

**Open Access** This article is licensed under a Creative Commons Attribution 4.0 International License, which permits use, sharing, adaptation, distribution and reproduction in any medium or format, as long as you give appropriate credit to the original author(s) and the source, provide a link to the Creative Commons licence, and indicate if changes were made. The images or other third party material in this article are included in the article's Creative Commons licence, unless indicated otherwise in a credit line to the material. If material is not included in the article's Creative Commons licence and your intended use is not permitted by statutory regulation or exceeds the permitted use, you will need to obtain permission directly from the copyright holder. To view a copy of this licence, visit <http://creativecommons.org/licenses/by/4.0/>.

#### References

- Adey RA, Pusch R (1999) Scale dependency in rock strength. *Eng Geol* 53:251–258
- Bahrani N, Kaiser PK (2016) Numerical investigation of the influence of specimen size on the unconfined strength of defected rocks. *Comput Geotech* 77:56–67. <https://doi.org/10.1016/j.compgeo.2016.04.004>
- Bahrani N, Kaiser PK, Valley B (2014) Distinct element method simulation of an analogue for a highly interlocked, non-persistently jointed rockmass. *Int J Rock Mech Min Sci* 71:117–130
- Bazant ZP (1984) Size effect in blunt fracture: concrete, rocks and metal. *Eng Mech* 110(4):518–535
- Bazant ZP (1997) Scaling of quasibrittle fracture: hypotheses of invasive and lacunar fractality, their critique and Weibull connection. *Int J Fract* 83:41–65
- Carpinteri A (1989) Decrease of apparent tensile and bending strength with specimen size: two different explanations based on fracture mechanics. *Int J Solids Struct* 25:407–429
- Carpinteri A, Chiaia B, Ferro G (1995) Size effects on nominal tensile strength of concrete structures: multifractality of material ligaments and dimensional transition from order to disorder. *Mater Struct* 28:311–317
- Castelli M, Saetta V, Scavia C (2003) Numerical study of scale effects on the stiffness modulus of rock masses. *Int J Geomech* 3(2):160–169
- Darlington WJ, Ranjith PG (2011) The effect of specimen size on strength and other properties in laboratory testing of

- rock and rock-like cementitious brittle materials. *Rock Mech Rock Eng* 44:513–529
- Dey T, Halleck P (1981) Some aspects of size-effect in rock failure. *Geophys Res Lett* 8(7):691–694
- Fan H, Li L, Zong P, Liu H, Yang L, Wang J, Yan P, Sun S (2023) Advanced stability analysis method for the tunnel face in jointed rock mass based on DFN-DEM. *Undrgrd Space* 13:136–149
- Fisher RA, Tippett LHC (1982) Limiting forms of the frequency distribution of the largest and smallest member of a sample. *Proc Cambridge Phil Soc* 24:180–190
- Hoek E, Brown ET (1980) *Underground excavations in rock*. Institution of Mining and Metallurgy, London
- Huang H, Detournay E (2008) Intrinsic length scales in tool-rock interaction. *Int J Geomech* 8:39–44
- Ma W, Xu Z, Chai J, Cao C, Wang Y (2023) Estimation of REV size of 2-D DFN models in nonlinear flow: Considering the fracture length-aperture correlation. *Comput Geotech* 161:105601
- Martin CD, Lu Y, Lan H (2011). Scale effects in a synthetic rock mass. In: Qian & Zhou (eds), *harmonizing rock engineering and the environment*. CRC Press, Boca Raton, 473–478
- Mogi K (1962) The influence of dimensions of specimens on the fracture strength of rocks. *Bull Earth Res Inst* 40:175–185
- Nomikos P, Kaklis K, Agioutantis Z, Mavrigiannakis S (2020) Experimental characterization and numerical modeling of the fracture process in banded Alfas porous stone. *Mat Design Process Comm*. <https://doi.org/10.1002/mdp2.165>
- Potyondy DO, Cundall PA (2004) A bonded-particle model for rock. *Int J Rock Mech Min Sci* 41(8):1329–1364
- Silva A, Azuaga L, Hennies WT (1993) A methodology for rock mass compressive strength characterization from laboratory tests. *Scale Effects in Rock Mass*. Balkema, Lisbon, pp 217–224
- Vardoulakis I, Kourkoulis SK, Exadaktylos GE, Rosakis A (2002) Mechanical properties and compatibility of natural building stones in ancient monuments: Dionysos marble. *Proceedings of the interdisciplinary workshop: The building stone in monuments*, Athens.
- Vileneuve MC, Diederichs M, Kaiser P (2012) Effects of grain scale heterogeneity on rock strength and the chipping process. *Int J Geomech* 12:632–647
- Wang S, Masoumi H, Oh J, Zhang S (2020). *Scale size and structural effects of rock materials*, Woodhead Publishing, ISBN 978-0-12-820031-5.
- Weibull W (1939) The phenomenon of rupture in solids. *Proc R Swed Inst Eng Res* 153:1–55
- Yiouta-Mitra P, Dimitriadis G, Nomikos P (2023) Size effect on triaxial strength of randomly fractured rock mass with discrete fracture network. *Bull Eng Geol Environ* 82:8
- Yoon J (2007) Application of experimental design and optimization to PFC model calibration in uniaxial compression simulation. *Int J Rock Mech Min Sci* 44(6):871–889
- Yoshinaka R, Osada M, Park H, Sasaki T, Sasaki K (2008) Practical determination of mechanical design parameters of intact rock considering scale effect. *Eng Geol* 96(3–4):173–186
- Zhang Q, Zhu H, Zhang L, Ding X (2011) Study of scale effect on intact rock strength using particle flow modeling. *Int J Rock Mech Min Sci* 48:1320–1328

**Publisher's Note** Springer Nature remains neutral with regard to jurisdictional claims in published maps and institutional affiliations.